Materials Horizons

ROYAL SOCIETY OF CHEMISTRY

COMMUNICATION

View Article Online
View Journal | View Issue

Check for updates

Cite this: *Mater. Horiz.*, 2023, 10, 3548

Received 16th September 2022,
Accepted 21st March 2023

DOI: 10.1039/d2mh01149b

rsc.li/materials-horizons

Published on 22 Mart 2023. Downloaded on 12.05.2026 22:31:39.

Soft–hard interface design in super-elastic conductive polymer hydrogel containing Prussian blue analogues to enable highly efficient electrochemical deionization†

Yifan Ren,‡[a] Fei Yu,‡[b] Xin-Gui Li,[a] Brian Yuliarto,[cd] Xingtao Xu,*[e] Yusuke Yamauchi *[fg] and Jie Ma *[a]

The poor cycling stability of faradaic materials owing to volume expansion and stress concentration during faradaic processes limits their use in large-scale electrochemical deionization (ECDI) applications. Herein, we developed a "soft–hard" interface by introducing conducting polymer hydrogels (CPHs), that is, polyvinyl alcohol/polypyrrole (PVA/PPy), to support the uniform distribution of Prussian blue analogues (*e.g.*, copper hexacyanoferrate (CuHCF)). In this design, the soft buffer layer of the hydrogel effectively alleviates the stress concentration of CuHCF during the ion-intercalation process, and the conductive skeleton of the hydrogel provides charge-transfer pathways for the electrochemical process. Notably, the engineered CuHCF@PVA/PPy demonstrates an excellent salt-adsorption capacity of 22.7 mg g^{-1} at 10 mA g^{-1}, fast salt-removal rate of 1.68 mg g^{-1} min^{-1} at 100 mA g^{-1}, and low energy consumption of 0.49 kW h kg^{-1}. More importantly, the material could maintain cycling stability with 90% capacity retention after 100 cycles, which is in good agreement with *in situ* X-ray diffraction tests and finite element simulations. This study provides a simple strategy to construct three-dimensional conductive polymer hydrogel structures to improve the desalination capacity and cycling stability of faradaic materials with universality and scalability, which promotes the development of high-performance electrodes for ECDI.

New concepts

Electrochemical deionization (ECDI) offers an energy-efficient way to provide affordable clean water. Faradaic materials have shown great potential for achieving higher ECDI performance than current benchmark carbon materials. Unfortunately, faradaic materials tend to have severely poor cycling stability due to the volume expansion and stress concentration of the faradaic material during the faradaic process, which limits their further application for practical ECDI. In this regard, it is highly desirable to develop strategies to address this problem, however they still remain in their infancy. In this demonstration, we first show the design of a soft–hard interface in faradaic ECDI electrodes through introducing conducting polymer hydrogels (CPHs), *i.e.*, polyvinyl alcohol/polypyrrole (PVA/PPy), as the support for uniform distribution of Prussian blue analogs (*e.g.*, copper hexacyanoferrate (CuHCF)). In the design, the soft buffer layer of the hydrogel could effectively alleviate the volume expansion of CuHCF during the ion intercalation process, and meanwhile, the conductive skeleton of the hydrogel will further provide the charge transfer pathways for the electrochemical process. As a consequence, the ECDI performance including desalination capacity and cycling stability of CuHCF has been significantly improved. This work is believed to provide an effective solution for addressing the limitations of faradaic electrodes.

Introduction

The freshwater crisis, caused by population growth and industrial expansion, has disrupted the harmonious development between humans and nature. At present, seawater desalination is an effective method to alleviate water shortages.[1] Traditional desalination technologies are based on membrane separation and phase thermal-change processes. However, electrochemical deionization (ECDI) technology has gradually attracted broad attention owing to its advantages of low energy consumption,

[a] *Research Center for Environmental Functional Materials, State Key Laboratory of Pollution Control and Resource Reuse, College of Environmental Science and Engineering, Tongji University, Shanghai 200092, P. R. China. E-mail: jma@tongji.edu.cn*
[b] *College of Marine Ecology and Environment, Shanghai Ocean University, Shanghai 201306, P. R. China*
[c] *Engineering Physics Department, Faculty of Industrial Technology, Institut Teknologi Bandung, Indonesia*
[d] *Research Center for Nanoscience and Nanotechnology, Institut Teknologi Bandung, Indonesia*
[e] *Research Center for Materials Nanoarchitectonics, National Institute for Materials Science, 1-1 Namiki, Tsukuba, Ibaraki 305-0044, Japan. E-mail: xingtao.xu@zjou.edu.cn*
[f] *School of Chemical Engineering and Australian Institute for Bioengineering and Nanotechnology (AIBN), The University of Queensland, Brisbane, Queensland 4072, Australia. E-mail: y.yamauchi@uq.edu.au*
[g] *Department of Materials Process Engineering, Graduate School of Engineering, Nagoya University, Nagoya, 464–8603, Japan*

† Electronic supplementary information (ESI) available. See DOI: https://doi.org/10.1039/d2mh01149b

‡ These authors contributed equally to this work.

This journal is © The Royal Society of Chemistry 2023

Published on 22 Mart 2023. Downloaded on 12.05.2026 22:31:39.

high efficiency, and no secondary pollution.[2–4] In general, ECDI can be divided into two categories according to the desalination mechanism: electric double-layer adsorption and faradaic reactions. ECDI is based on the concept of capacitive deionization, but it expands the range of electrode materials to form various electrochemical desalination systems through various combinations.[5–7] In 1996, Farmer *et al.*[8] utilized a carbon aerogel to remove NaCl from water and achieved a significant increase in desalination capacity. Since then, ECDI has undergone a period of rapid development.

Electrode materials are crucial to the operation of ECDI systems. Developing systems with a high capacity, rapid rate, and excellent electrode stability is necessary to promote the progress of ECDI technology.[9] In 2012, Pasta *et al.*[10] proposed the use of sodium manganese oxide ($Na_{2-x}Mn_5O_{10}$) and silver as the cathode and anode used to capture NaCl, respectively. This expanded the storage principle of ECDI from an electric double-layer adsorption to a faradaic reaction, which effectively mitigated the side reaction and co-ionic effect owing to the use of carbon materials and greatly improved the adsorption capacity of existing ECDI systems.[11] Subsequently, various faradaic materials have been used in ECDI systems, particularly battery materials such as transition metal oxides,[12,13] Prussian blue analogues (PBAs),[14,15] and polyanionic phosphates.[16] PBAs are a class of coordination compounds that can realise rapid and reversible ion intercalation/de-intercalation owing to their open-frame structure, large ion channel, and high redox potential.[17] In ECDI, Na^+ can be stored and diffuses into the nanoscale interspaces of a cross skeleton formed by transition metals and cyano-ligands.[18]

Although battery materials exhibit a high desalination capacity, the lattice change that occurs in the ion-insertion/extraction process can lead to volume expansion. This results in particle breakage and structural changes, which significantly affect the service life of the electrode. In addition, ECDI systems under aqueous conditions have higher requirements for electrode-material stability. For PBAs, the strain that accumulates between nanoparticles in the charging and discharging processes is difficult to release. This causes stress concentration and structural damage in PBAs, and decreases their stability.[19,20]

In view of the above electrode-failure phenomenon, several optimization strategies, such as surface coating and hollow-structure design strategies, have been proposed to improve the stability of PBAs.[18,21] Park *et al.*[22] reported the use of a graphene oxide-coated Prussian blue (PB-GO) electrode material. Compared with pristine PB, PB-GO exhibited an excellent rate performance, with a capacity retention rate as high as 78.8% after 10 000 cycles. Surface coatings can enhance PBA stability; however, the coating thickness is difficult to control. When the thickness is greater than 10 nm, the coating layer inhibits contact between the electrolyte and PBAs, limits the rapid migration of ions, and reduces the desalination capacity. Wan *et al.*[23] designed a gradually hollow PBA nanoframe and composited it with carbon nanotubes; the resulting capacity-retention rate reached 92% after 500 cycles. This hollow hierarchical configuration improves the lattice tolerance and reduces the number of sodium diffusion paths, thereby resulting in excellent rate capability and cycling stability. However, the preparation of hollow structures typically requires a sacrificial template or acid–base etching, which, to some extent, leads to the collapse and destruction of the product structure, thereby suppressing the performance of the electrode.

Conductive polymer hydrogels (CPHs) are a special class of smart hydrogels that perfectly combine the remarkable strengths of conductive materials and hydrogels. They have excellent mechanical properties and three-dimensional (3D) network structures, which are conducive to fast electron and ion transport.[24–26] In addition, the elastic modulus of CPHs provides a buffer layer that accommodates the stress concentration induced by volume expansion, thereby preventing the structure from collapsing while withstanding strong water impact and maintaining the overall electrode structure.[27,28] Therefore, combining CPHs with battery materials to construct ECDI electrodes is a feasible approach. However, to our knowledge, no related studies have been published on this approach.

In this study, we developed a novel hydrogel electrode with outstanding performance using a ''soft–hard'' interface design that comprises a composite of CuHCF and polyvinyl alcohol/polypyrrole CPH (CuHCF@PVA/PPy). The hydrogel possesses superior electrical conductivity, mechanical properties, and biocompatibility. The uniform and continuous hierarchical porous structure provides abundant electrochemical active sites and avoids the agglomeration of CuHCF, and the buffering effect of the ''soft layer'' improves the lattice strain of the CuHCF particles and enhances the cycling stability of the electrode. The assembled asymmetric CuHCF@PVA/PPy//AC cell benefits from the rational structural design and improved electrochemical conductivity and exhibits a superior desalination capacity (22.7 mg g^{-1}) and long cycle stability (90% after 100 cycles). The design of 3D composite CPHs expands the material utilisation rate, effectively relieves stress concentration, and improves the cycle life of the electrode, and this approach can be extended to other faradaic electrode materials.

Results and discussion

Synthesis and characterization of CuHCF@PVA/PPy

The preparation procedure for CuHCF@PVA/PPy is briefly illustrated in Fig. 1a. The PVA surface contains a large number of hydroxyl groups as active sites, which interact with the imino group in the pyrrole ring *via* hydrogen bonding, and the pyrrole monomer is adsorbed on the PVA surface. Under the oxidation of ammonium persulfate, the pyrrole monomer is oxidatively polymerized into PPy, and a conductive layer is finally formed on the surface of the PVA. PPy is uniformly distributed among the PVA owing to the *in situ* polymerization, which is beneficial for increasing the conductivity of the PVA skeleton.[29] Moreover, when the $Cu(NO_3)_2$ solution is mixed with the PVA/PPy solution, the hydroxyl groups in PVA can also adsorb Cu^{2+} through electrostatic interactions and act as nucleation sites to form uniformly distributed CuHCF particles. Finally, multiple freeze–thaw

Published on 22 Mart 2023. Downloaded on 12.05.2026 22:31:39.

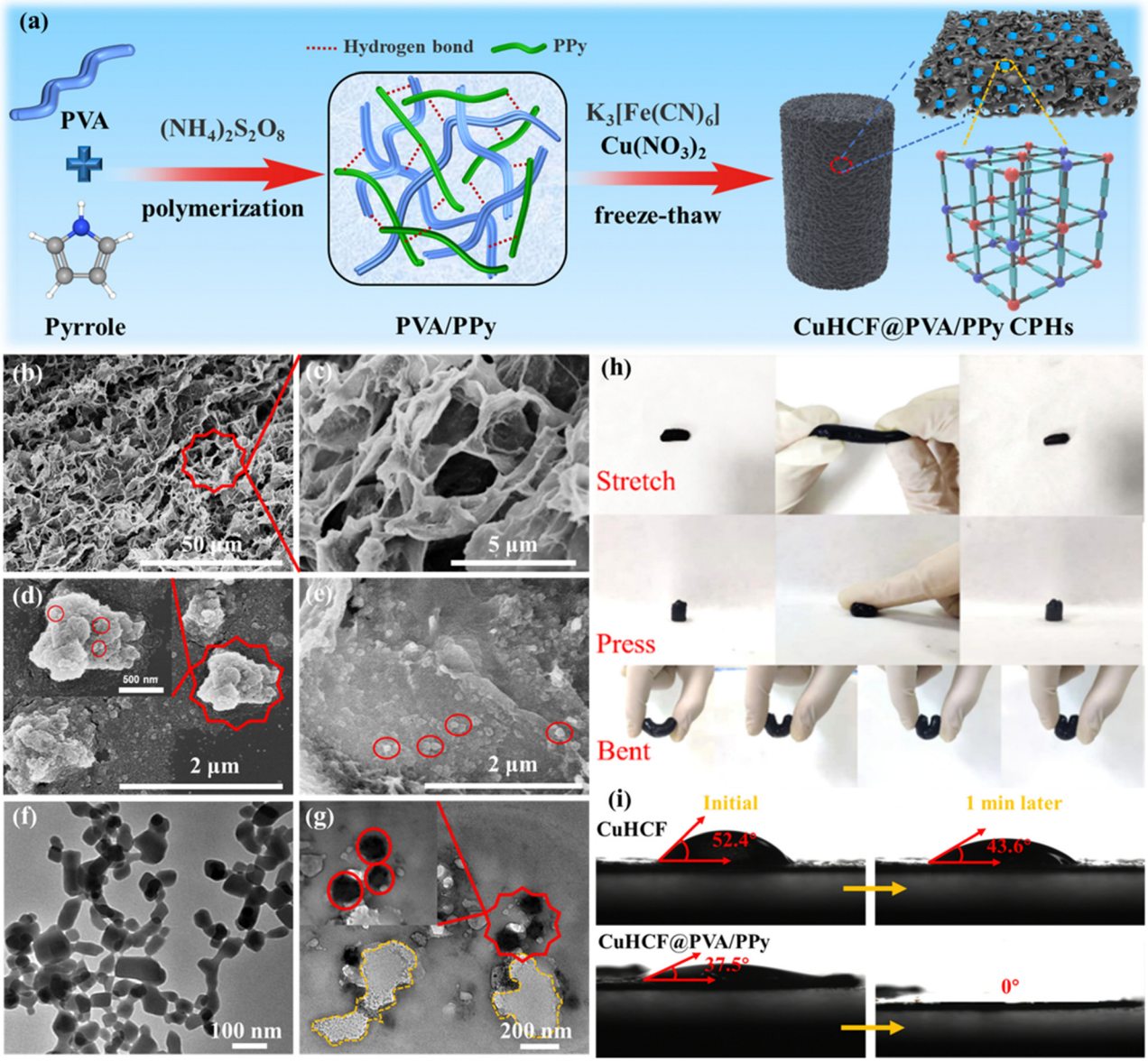

Fig. 1 (a) Illustration of CuHCF@PVA/PPy synthesis process. (b and c) SEM images of CuHCF@PVA/PPy under different resolutions. High magnification SEM images of (d) CuHCF particles and (e) CuHCF@PVA/PPy. TEM images of (f) CuHCF particles and (g) CuHCF@PVA/PPy. (h) Photograph of CuHCF@PVA/PPy with mechanical transformation. (i) Variation of water contact angles on the surface of CuHCF and CuHCF@PVA/PPy after 1 min.

processes promote the formation of the PVA network skeleton, which results in hydrogels with excellent mechanical properties.

Scanning electron microscopy (SEM) images of CuHCF@PVA/PPy show a loosely sponge-like 3D porous structure with numerous wrinkles (Fig. 1b). The surface of the hydrogel is coarse, and the pores are mainly at the macroscale; therefore, the hydrogel exhibits a large internal space, accommodates a large amount of water, and displays strong wettability (Fig. 1c). The CuHCF nanoparticles clump together to form discrete micron-scale hills (Fig. 1d). However, when CuHCF is warped by the PVA/PPy conductive polymer, the CuHCF particles are distributed separately in the PPy/PVA skeleton, which is ascribed to the *in situ* growth of CuHCF particles on the PVA chains. (Fig. 1e). Similar results are obtained using transmission electron microscopy (TEM). Fig. 1f reveals that CuHCF stacks together, and the size of the particles is randomly distributed, which results in a low material-utilization efficiency. However, the TEM image of CuHCF@PVA/PPy confirms that the conductive gel not only plays a crucial role in guiding the nucleation of CuHCF, but also effectively reduces the particle size and uniformly distributes CuHCF in the three-dimensional conductive skeleton (Fig. 1g). All the aforementioned structural properties of CuHCF@PVA/PPy are beneficial for improving the utilization efficiency of the materials and promoting the rapid migration of Na^+ in the hydrogel.

Additionally, the 3D multichannel structures enable excellent mechanical stability in CuHCF@PVA/PPy. The hydrogel can be stretched, pressed, and bent without observable crevices, and it

 This journal is © The Royal Society of Chemistry 2023

Published on 22 Mart 2023. Downloaded on 12.05.2026 22:31:39.

can quickly return to its original form (Fig. 1h). The reversible mechanical properties can be explained as follows. (1) The hydroxyl groups of PVA develop network and sustain the hydrogel.[30] (2) CuHCF@PVA/PPy is filled with water and gas within its porous spaces, which can be released to prevent deformation of the hydrogel when subjected to external pressure.[29] The remarkable mechanical strength of the hydrogel is beneficial for maintaining the macroscopic stability of the electrode, which can withstand high flow velocity. Good wetting ability can promote the diffusion of Na^+ to the electrode surface and interior, thereby achieving fast transmission. The hydrophilicity of the as-prepared samples was measured using a dynamic water contact (Fig. 1i). The initial contact angles of CuHCF and CuHCF@PVA/PPy are 52.35° and 37.53°, respectively. After 1 min, the contact angles of both materials decrease; however, water droplets are not observed on the surface of CuHCF@PVA/PPy, which indicates its good hydrophilicity. This may be related to the hydroxyl functional groups on PVA and the loose and porous structural features of the hydrogel.

The stress–strain curves of CuHCF@PVA/PPy are shown in Fig. 2a to further evaluate its mechanical performance. The hydrogel is able to achieve a 60% strain with a proportional deformation displacement, and it almost recovers its previous morphology after the force is released. The results of the ten-cycle compression experiment show that when the deformation exceeds 55%, the hydrogel can still quickly return to its initial state without significant changes (Fig. S1 and Video S1, ESI†). This reveals that the hydrogel demonstrates excellent mechanical properties and will not crack or fall off during the desalination process.

The crystallographic structures of the CuHCF particles and CuHCF@PVA/PPy were confirmed using X-ray diffraction (XRD). Most of the diffraction peaks of both electrode materials are consistent with the typical pattern of CuHCF with only a minor deviation (Fig. 2b). However, it should be noted that a 2θ value of 19° indicates the characteristic peak of PVA, whereas a broad peak appears between 20° and 25°, thereby indicating the existence of PPy.[29,31]

The chemical composition and elemental valence state of the hydrogel are studied using X-ray photoelectron spectroscopy (XPS). The high-resolution C 1s spectrum is fitted with two peaks at 284.7 and 286.4 eV, which correspond to C–C/C≡N and C–N/C–O, respectively (Fig. 2c).[20] As shown in Fig. 2d, the main peak in the N 1s spectrum is located at 397.9 eV, which is attributed to the C≡N bond.[32] The higher binding energies of 399.9 and 402.1 eV correspond to pyrrolic N and graphitic N, respectively.[33] The Fe 2p region shows two peaks at 708.4 and 721.4 eV, which are attributed to the Fe $2p_{3/2}$ and Fe $2p_{1/2}$ spin orbitals of Fe^{2+}, respectively (Fig. 2e). In addition, two peaks detected at 709.8 and 723.4 eV indicate the Fe $2p_{3/2}$ and Fe $2p_{1/2}$ spin orbitals of Fe^{3+}, respectively. The two satellite features at 714.2 and 719.4 eV correspond to Fe^{2+} and Fe^{3+}, respectively.[20,34] For Cu^+ and Cu^{2+}, the Cu $2p_{3/2}$ peak is deconvoluted into two peaks centered at 933.1 and 935.4 eV, respectively (Fig. 2f).[35] For the Cu $2p_{1/2}$ spin orbits, the peak positions of Cu^+ and Cu^{2+} are at 952.9 and 954.9 eV, respectively.[35] The thermal stability of CuHCF@PVA/PPy was further investigated using thermogravimetric analysis (TGA) under an O_2 atmosphere (Fig. S2, ESI†). The results show that the weight loss is divided into three steps. When the

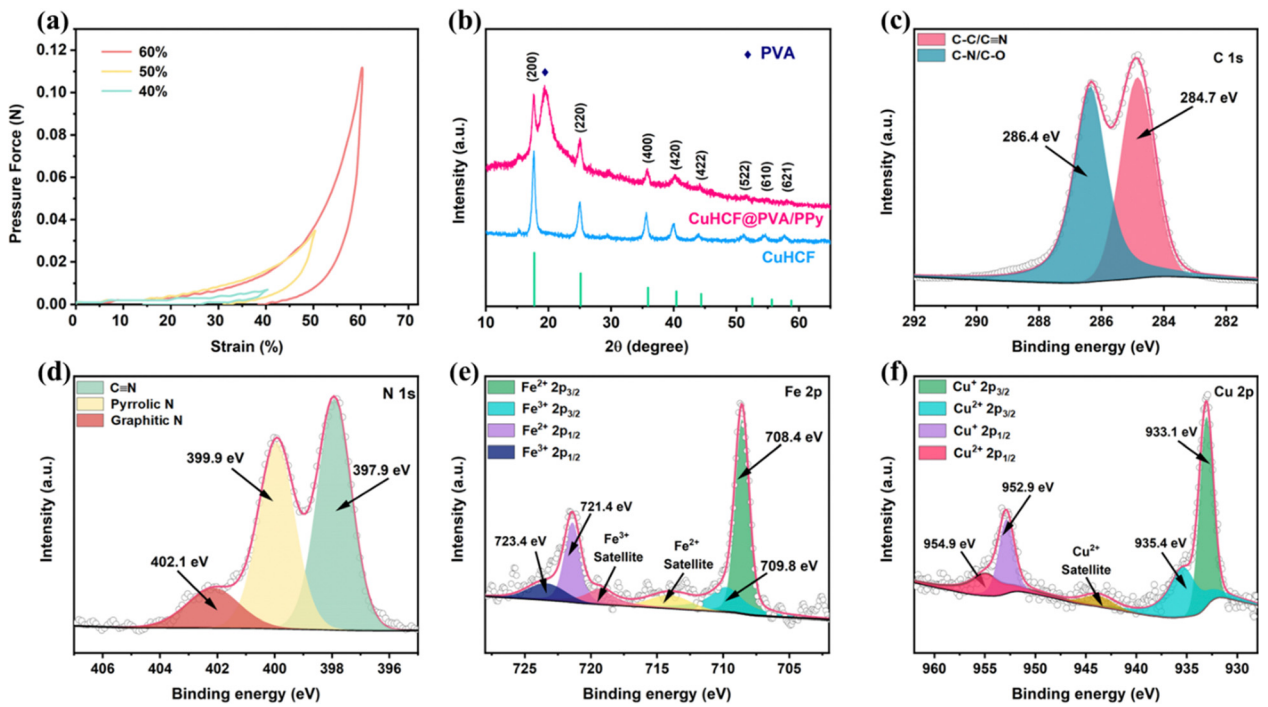

Fig. 2 (a) The stress *vs.* strain curves of CuHCF@PVA/PPy. (b) XRD patterns of CuHCF and CuHCF@PVA/PPy. High-resolution XPS spectra of (c) C 1s, (d) N 1s, (e) Fe 2p, and (f) Cu 2p for CuHCF@PVA/PPy.

Published on 22 Mart 2023. Downloaded on 12.05.2026 22:31:39.

temperature increases from 25 to 213 °C, the weight loss is 12.5%, owing to the evaporation of adsorbed water and crystal water, of which crystal water accounts for a 6.4% weight loss. The second step is the decomposition of the CuHCF structure and its conversion to Fe_2O_3 and CuO at approximately 335 °C; the TGA curve shows a significant loss of 41.1%. Finally, when the temperature reaches 460 °C, PVA and PPy are converted into CO_2 and H_2O owing to oxidation, and the weight loss is 36.6%. Therefore, the above characterization confirmed the formation of CuHCF and the successfully preparation of CuHCF@PVA/PPy.

Electrochemical characterization

The electrochemical performances of CuHCF@PVA/PPy and CuHCF were studied in a three-electrode device using 1 M NaCl as the electrolyte to highlight their structural advantages. Cyclic voltammetry (CV) was employed to investigate the electrochemical changes in the as-prepared samples during Na^+ insertion/extraction.[36,37] Fig. 3a shows the CV curves of CuHCF@PVA/PPy at different scan rates. It can be observed that when the scan rate is 1 mV s^{-1}, a pair of redox peaks appear at 0.48 V/0.5 V, which are similar to the peak positions of pure CuHCF (Fig. S3a, ESI†). This is attributed to the redox reaction of Fe^{3+}/Fe^{2+} and confirms the existence of the (de)intercalation mechanism within CuHCF crystals.[38] When the scan rate increases, the redox peaks weaken or even disappear owing to the shortened reaction time. The CV curves for a selection of 50 cycles are shown in Fig. 3b and Fig. S3b (ESI†). The CV curve of CuHCF shows a significant deviation after 50 cycles. This indicates the collapse and disruption of its framework during multiple insertions/de-insertions of Na^+, which leads to capacity decay. In contrast, the CV curve of CuHCF@PVA/PPy exhibits only a slight shift after 50 cycles. This phenomenon reveals that the long cycle stability of CuHCF@PVA/PPy is superior to that of CuHCF because the hydrogel flexible skeleton provides CuHCF with a buffer that releases strain during the charge/discharge process.

Moreover, galvanostatic charge–discharge (GCD) curves are used to quantitatively evaluate the capacities of both samples at various specific currents. In contrast to CuHCF, the curve of the hydrogel does not exhibit a clear platform voltage, thereby indicating that pseudocapacitance behaviour plays an important role in the charge–discharge process. Therefore, the storage of Na^+ is primarily owing to the redox reaction on the surface of CuHCF, which is not limited by the slow kinetics of solid-phase ion diffusion. Thus, a high desalination rate can be achieved (Fig. 3c).[39] Additionally, the curves of specific charge capacity *vs.* cycles (100 mA g^{-1}) clearly show that CuHCF@PVA/PPy can still maintain a charge-capacity retention rate of 96.5% after 60 cycles, whereas that of CuHCF decreases to 64.3% (Fig. 3d). This indicates that the hydrogel structure realises the uniform distribution of CuHCF and improves its utilisation efficiency. It also effectively relieves the stress concentration of CuHCF and enhances its cycling stability. The improved electrochemical performance of CuHCF@PVA/PPy was further investigated using electrochemical impedance spectroscopy (Fig. 3e). The obtained Nyquist plots present a quasi-semicircle in the

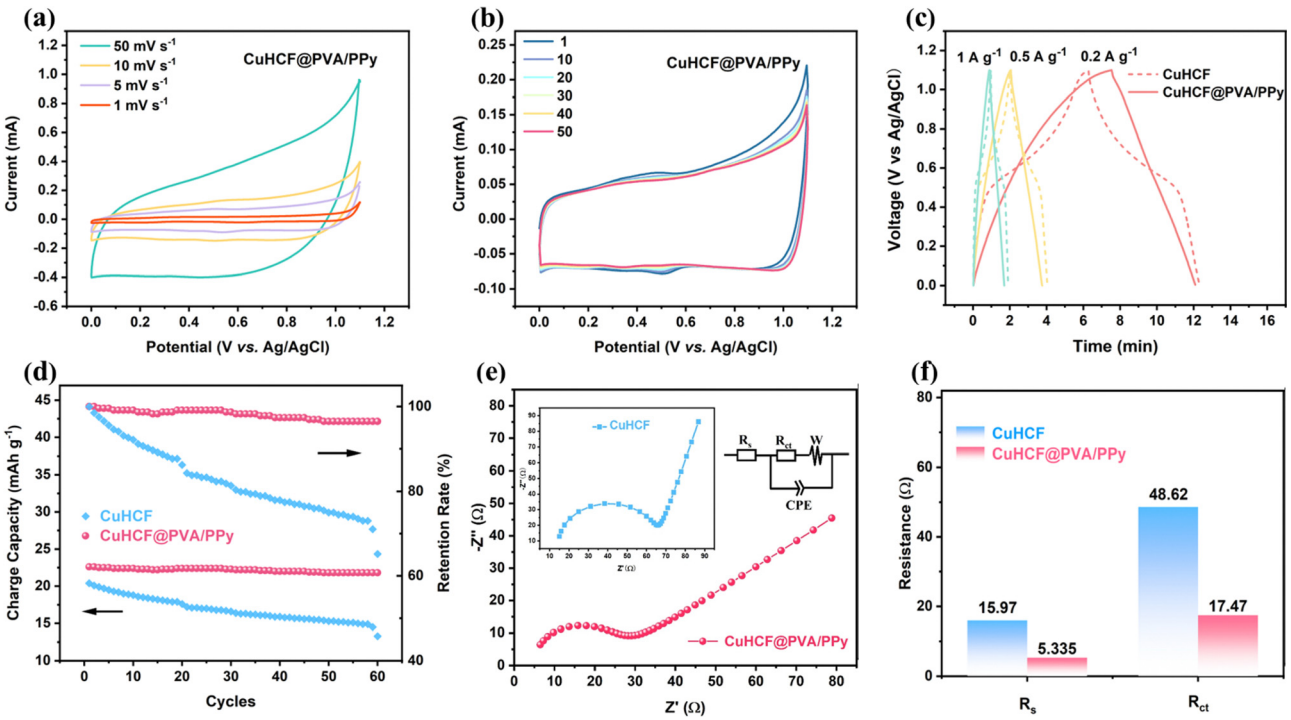

Fig. 3 (a) CV curves of CuHCF@PVA/PPy in 1 M NaCl solution under different scan rates. (b) CV curves of CuHCF@PVA/PPy under a scan rate of 1 mV s^{-1} for 50 cycles. (c) GCD curves of CuHCF and CuHCF@PVA/PPy at different specific currents. (d) The capacities and retention rate of CuHCF and CuHCF@PVA/PPy after 60 cycles. (e) Nyquist plot with an inset showing the equivalent circuit and the (f) fitting results of CuHCF and CuHCF@PVA/PPy.

 This journal is © The Royal Society of Chemistry 2023

Published on 22 Mart 2023. Downloaded on 12.05.2026 22:31:39.

high-frequency region and a straight-line segment in the low-frequency region, which mainly correspond to the charge-transfer resistance (R_{ct}) and Warburg diffusion impedance (W), respectively. A suitable equivalent-circuit diagram is selected for fitting, where R_s and CPE represent the equivalent series resistance and constant phase element part, respectively. The fitting results in Fig. 3f show that the R_s and R_{ct} values of CuHCF@PVA/PPy are considerably smaller than those of CuHCF. The low R_{ct} and R_s values are obtained because PPy serves as the conductive polymer that increases the conductivity of CuHCF, and PVA works as a skeleton to mitigate the aggregation of CuHCF particles. Moreover, the small resistance benefits a fast desalination rate and low energy consumption because the resulting conductivity favours Na^+ transportation during the charge and discharge processes.[40] The excellent electrochemical performance and reversible sodium-storage ability prompted us to further investigate the application of CuHCF@PVA/PPy in desalination.

Desalination performance

The desalination performance of CuHCF@PVA/PPy under different conditions was investigated using a hybrid ECDI cell (Fig. S4, ESI†). When a forward current is applied, the voltage between the two poles of the device gradually increases, which corresponds to the capturing of Na^+ in the cathode and Cl^- in the anode (Fig. 4a).[41] The specific current is an essential operating parameter in ECDI that is closely related to desalination efficiency and energy consumption. Fig. 4b shows that the salt-adsorption capacity of CuHCF@PVA/PPy is 22.11 mg g^{-1} at 10 mA g^{-1} (cut-off voltage: −1 to 1 V), and the capacity gradually decreases with increasing specific current (Fig. S5, ESI†). This is because a large specific current promotes a shorter charging time and greater diffusion confinement, which leads to a decrease in the desalination capacity.[42,43]

Fig. 4c compares the desalination performances of the two electrodes at different specific currents. The desalination capacity of CuHCF@PVA/PPy is 14 mg g^{-1} at 50 mA g^{-1}, which is higher than that of CuHCF (12.6 mg g^{-1}) under the same conditions. The salt adsorption rates of the two samples gradually increase with increasing specific current, but that of CuHCF@PVA/PPy is always higher (1.68 mg g^{-1} min^{-1} at 100 mA g^{-1}). Under a fixed specific current of 50 mA g^{-1}, the desalination capacities of the two materials were investigated under different cut-off voltages (Fig. 4d). When the voltage range extends from −0.8 V/+0.8 V to −1.2 V/+1.2 V, the capacity of CuHCF@PVA/PPy improves from 7.5 to 20.2 mg g^{-1}. The increase in the cut-off voltage enables the electrode to obtain more charge for the desalination reaction, thereby achieving high-efficiency desalination. Compared with CuHCF, CuHCF@PVA/PPy exhibits a better desalination capacity at any cut-off voltage. To fully utilise the desalination performance of the gel, the power-supply operation was changed to a constant-voltage mode, and desalination was investigated for different voltage ranges. When the voltage increases from 1 to 1.6 V, the capacity of CuHCF@PVA/PPy increases from 19.02 to 59.03 mg g^{-1}. This increase is primarily owing to the increased electrostatic driving force, which enhances the embedding of Na^+ in the CuHCF framework (Fig. S6 and S7, ESI†). Notably, the constructed CuHCF@PVA/PPy hydrogels exhibit excellent salt-adsorption capacities and rates compared to those of previously reported carbon-based and faradaic electrodes (Fig. S8, ESI†).[44–54] This can be ascribed to the hierarchical porous skeleton formed by the PVA framework, which enables the fast transport of water-carrying ions between the mesopores and micropores. Furthermore, the PPy conductive network is conducive to improving the electron- and ion-transport rate, and it effectively alleviates the volume expansion of CuHCF during Na^+ storage as part of the soft interface. Besides, pure PVA/PPy gels were synthesized and tested for comparison. The results showed that the capacity of PVA/PPy gels under constant voltage conditions was much lower than that of CuHCF@PVA/PPy (Fig. S9, ESI†). Therefore, the desalination performance of the gel should be jointly determined by PVA/PPy and CuHCF, where CuHCF can achieve the main adsorption of Na^+ through redox ion intercalation reaction, while PVA/PPy will support the adsorption of Na^+ through electrostatic force. Notably, the desalination ability of the hydrogel is also closely related to the content of active material (CuHCF) it contains. When the amount of CuHCF increases, the desalination capacity also improves accordingly.[55]

Energy consumption and recovery during desalination is a critical parameter in engineering practice, and the process can be divided into two successive charge–discharge cycles (Fig. S10, ESI†). The specific current (Fig. 4e) and cut-off voltage (Fig. S11, ESI†) were changed to explore the energy consumption and recovery of the hydrogel and CuHCF, respectively. As these two variables increase, the energy consumptions of both materials exhibit an upward trend; however, the energy consumption of the hydrogel is significantly lower than that of CuHCF. In addition, the hydrogels perform better in the energy-recovery process, which indicates that less energy is consumed during the entire process. For example, CuHCF@PVA/PPy has an energy consumption of 0.49 kW h kg^{-1} with an energy recovery of 31.81% (100 mA g^{-1}). In contrast, the energy consumption of CuHCF can be as high as 0.69 kW h kg^{-1}, and the energy recovery is only 14.36%. This is mainly because the self-supported film electrodes possess a prominent advantage over the coated film electrode. However, a 3D binder-free hydrogel can reduce the unrecovered energy owing to the absence of binder additives, and it can enhance the desalination capacity because the uniform distribution of inorganic faradaic-material particles among the organic hydrogel can alleviate aggregation. Therefore, CuHCF@PVA/PPy has a higher salt-removal capacity and rate, and it consumes less energy.

The cyclic stability of electrode is very important for practical application. Hu *et al.* reported a CuHCF with high desalination capacity and good cyclic stability because of the suitable P/N charge ratio to keep the electrode within the appropriate potential range.[56] In this article, through the coating strategy of soft–hard interface design, CuHCF@PVA/PPy exhibits an average desalination performance (45 mg g^{-1}) with a capacity retention rate of 90% after 100 cycles (10 mA g^{-1}, −1.2 to 1.2 V), which indicates a better cyclic stability than that of pure CuHCF

Published on 22 Mart 2023. Downloaded on 12.05.2026 22:31:39.

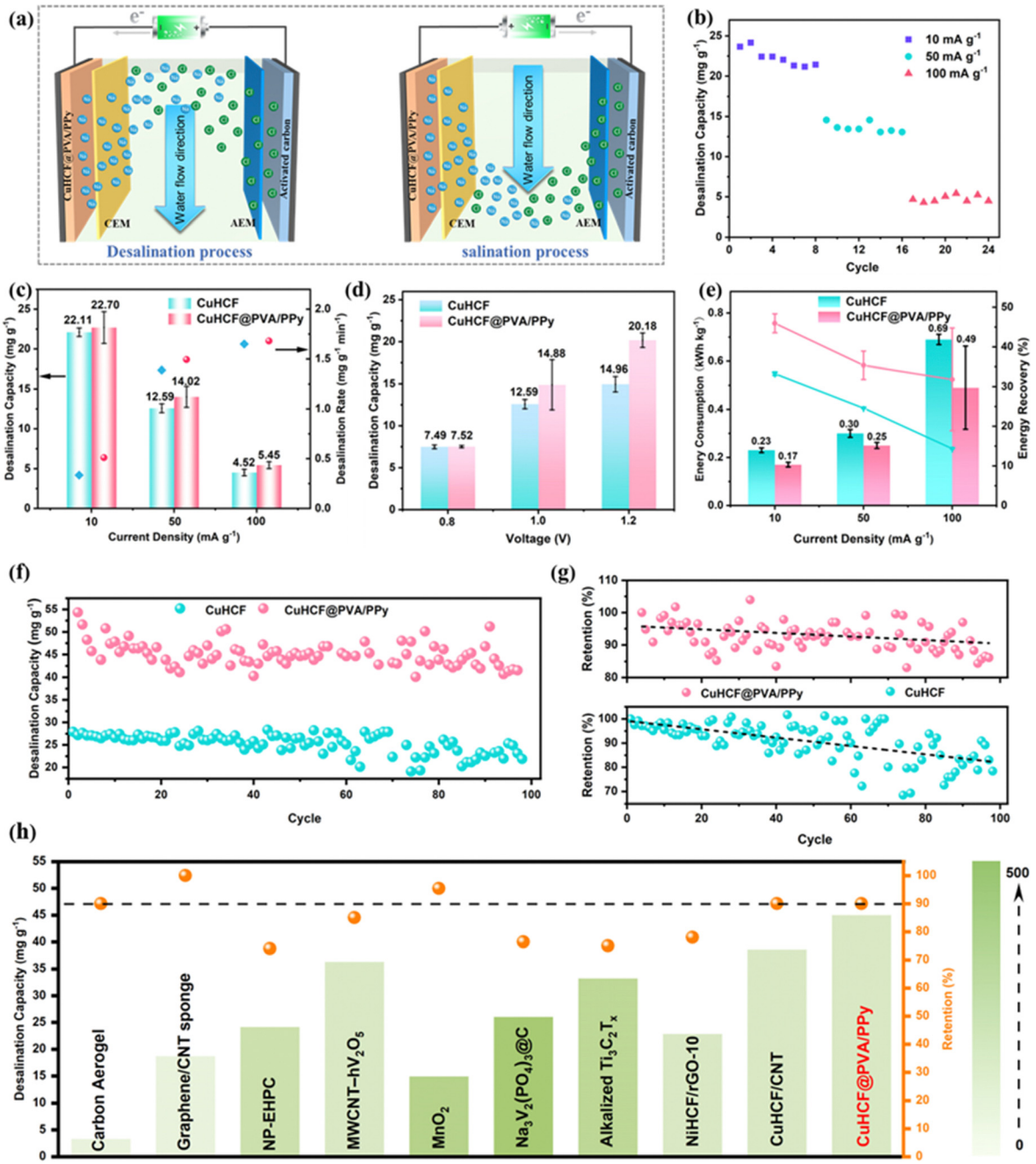

Fig. 4 (a) Schematic of the CuHCF@PVA/PPy||AC ECDI process. (b) Salt-adsorption capacity of CuHCF@PVA/PPy at various specific currents (cut-off voltage: −1 to 1 V). (c) Comparison of salt-adsorption capacities and rates of CuHCF and CuHCF@PVA/PPy at different specific currents (cut-off voltage: −1 to 1 V). (d) Salt-adsorption capacities of CuHCF and CuHCF@PVA/PPy at various cut-off voltages (specific current: 50 mA g^{-1}). (e) Energy consumption and recovery of CuHCF and CuHCF@PVA/PPy at various specific currents. (f) Cycling performances and (g) capacity-retention values of the CuHCF and CuHCF@PVA/PPy electrodes at a specific current of 10 mA g^{-1} (cut-off voltage: −1.2 to 1.2 V). (h) Cyclic stability comparison of various electrode materials considering final capacity, retention rate, and cycle number (a different color represents the cycle number).[46,52,56–62]

(Fig. 4f and g). Besides, compared with other carbon-metal composite electrodes, CuHCF@PVA/PPy demonstrates a high capacity and good stability simultaneously (Fig. 4h and Table S1, ESI†).[46,52,56–62] Moreover, the XRD pattern of CuHCF@PVA/PPy after 100 cycles shows only a slight deviation in the XRD pattern with a small NaCl peak (Fig. S12, ESI†). Moreover, the macro-scale versions of the two electrode types show that the CuHCF particles are attached to the cation exchange membrane (CEM) and eroded owing to water flow. However, the CEM of the CuHCF@PVA/PPy electrode still retains suitable shapes, which indicates the excellent stability of the hydrogel (Fig. S13, ESI†).

The CuHCF@PVA/PPy hydrogel exhibits exceptional desalination and energy-consumption performances, which can be ascribed to the following features: (1) the hierarchically 3D PVA

 This journal is © The Royal Society of Chemistry 2023

Published on 22 Mart 2023. Downloaded on 12.05.2026 22:31:39.

and PPy hydrogel alleviates the aggregation of CuHCF particles, and the mesopore and macropore structure enables fast ion transport and enhances the salt-adsorption rate; (2) the conductive network of PPy improves the conductivity of CuHCF and reduces the resistance of the hydrogel, thereby achieving a reduction in energy consumption; (3) compared with CuHCF, the soft interfacial buffer layer of the hydrogel effectively alleviates the stress concentration of CuHCF particles during the process of Na^+ storage, and the hydrogel demonstrates good cycle stability in electrochemical and desalination tests; and (4) the strong interaction between PPy and the PVA polymer chains also enhances the mechanical properties of the hydrogel and prevents water erosion. Therefore, improvement in the cyclic stability of the CuHCF@PVA/PPy hydrogel is achieved from both macroscopic and microscopic perspectives.

Desalination mechanism

The electrode capacity is typically composed of Na^+-ion diffusion-controlled and capacitance processes. To reveal the desalination process of CuHCF@PVA/PPy, the power law relation (eqn (S5)–(S7), ESI†) between the current and sweep speed is confirmed based on the CV curves. Generally, a *b*-value of 0.5 represents a diffusion-controlled faradaic reaction, and a *b*-value of 1.0 indicates perfect capacitive behaviour.[63] As shown in Fig. 5a, four regions of the CV curve (potential 0.3, 0.5 (cathode and anode), and 0.9 V) are selected, and the corresponding *b*-values are calculated as 0.71, 0.77, 0.79, and 0.78, respectively. According to Fig. 5b, the capacitance improves gradually as the scan rates increase, which reflects a rate-limited diffusion process.[64,65] For example, the hydrogel has a capacitance contribution ratio of 63% at 50 mV s^{-1} (Fig. 5c). These results demonstrate that the diffusion-controlled behaviour and capacitive behaviour jointly promote the intercalation of Na^+ in CuHCF@PVA/PPy, thereby achieving an outstanding desalination capacity and rate.

To further explore the desalination mechanism, an *in situ* device similar to a coin cell was constructed and characterised using *in situ* XRD, as shown in Fig. 5d and Fig. S14 (ESI†). A voltage range of −0.9 to 0.9 V and a low current density of 20 mA g^{-1} were chosen to provide sufficient time to achieve the complete insertion/extraction of Na^+. Fig. 5e shows the selected range of the *in situ* XRD patterns of CuHCF@PVA/PPy at different charge–discharge stages. The typical diffraction peaks located at (400) and (420) from the CuHCF crystals shift to lower angles during desalination and return to their original angles after electrode regeneration, which is due to the reversible intercalation/de-intercalation of Na^+ in CuHCF.[15,66] The change in the peak position in the XRD results clearly demonstrates the high reversibility and stable electrochemical properties of the CuHCF@PVA/PPy electrode, which plays a crucial role in desalination.

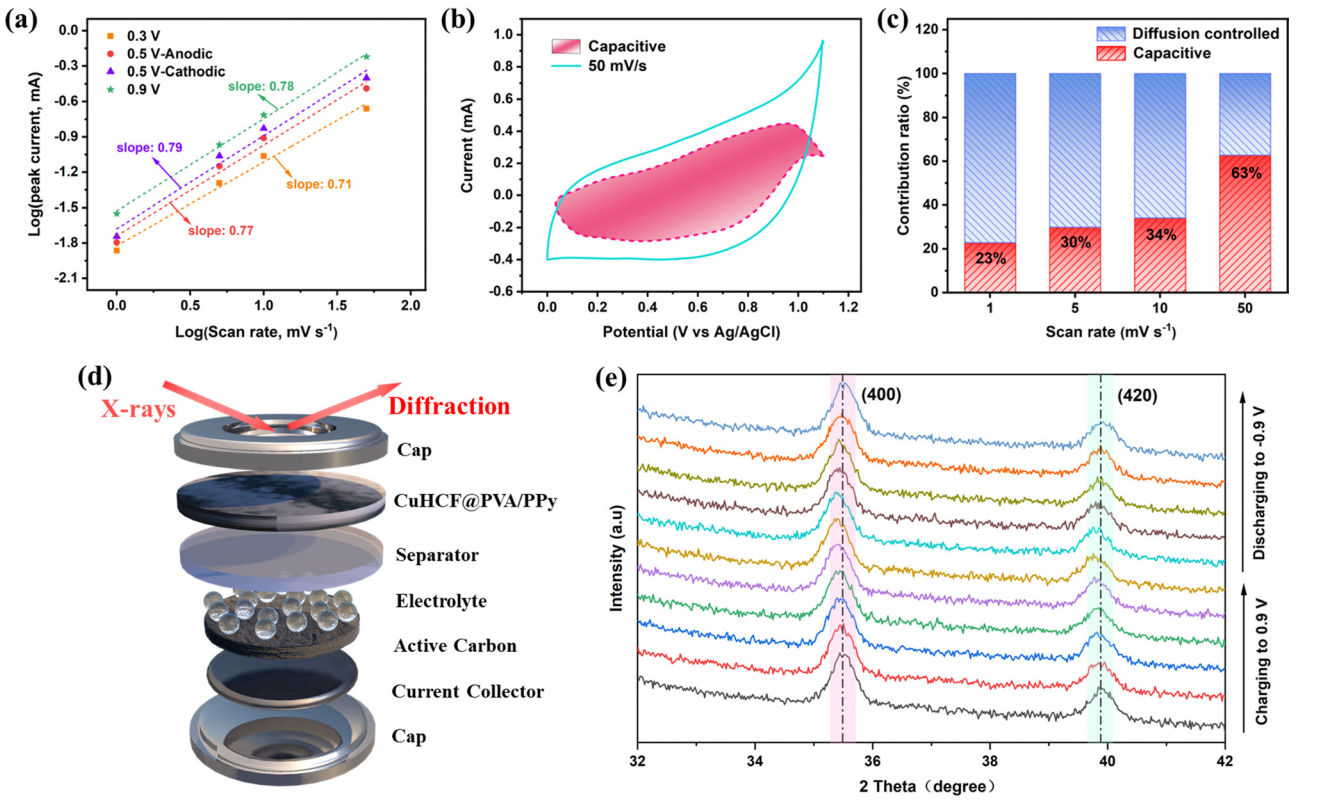

Fig. 5 (a) Determination of *b*-values for various selected regions for CuHCF@PVA/PPy. (b) Capacitive contribution of CuHCF@PVA/PPy at a scan rate of 50 mV s^{-1}. (c) Diffusion-limited and capacitive contributions to the total capacity of CuHCF@PVA/PPy at different scan rates. (d) Schematics of the customised XRD cell for *in situ* measurements. (e) *In situ* XRD patterns of the CuHCF@PVA/PPy cell during the desalination/regeneration process at a specific current of 20 mA g^{-1}.

Published on 22 Mart 2023. Downloaded on 12.05.2026 22:31:39.

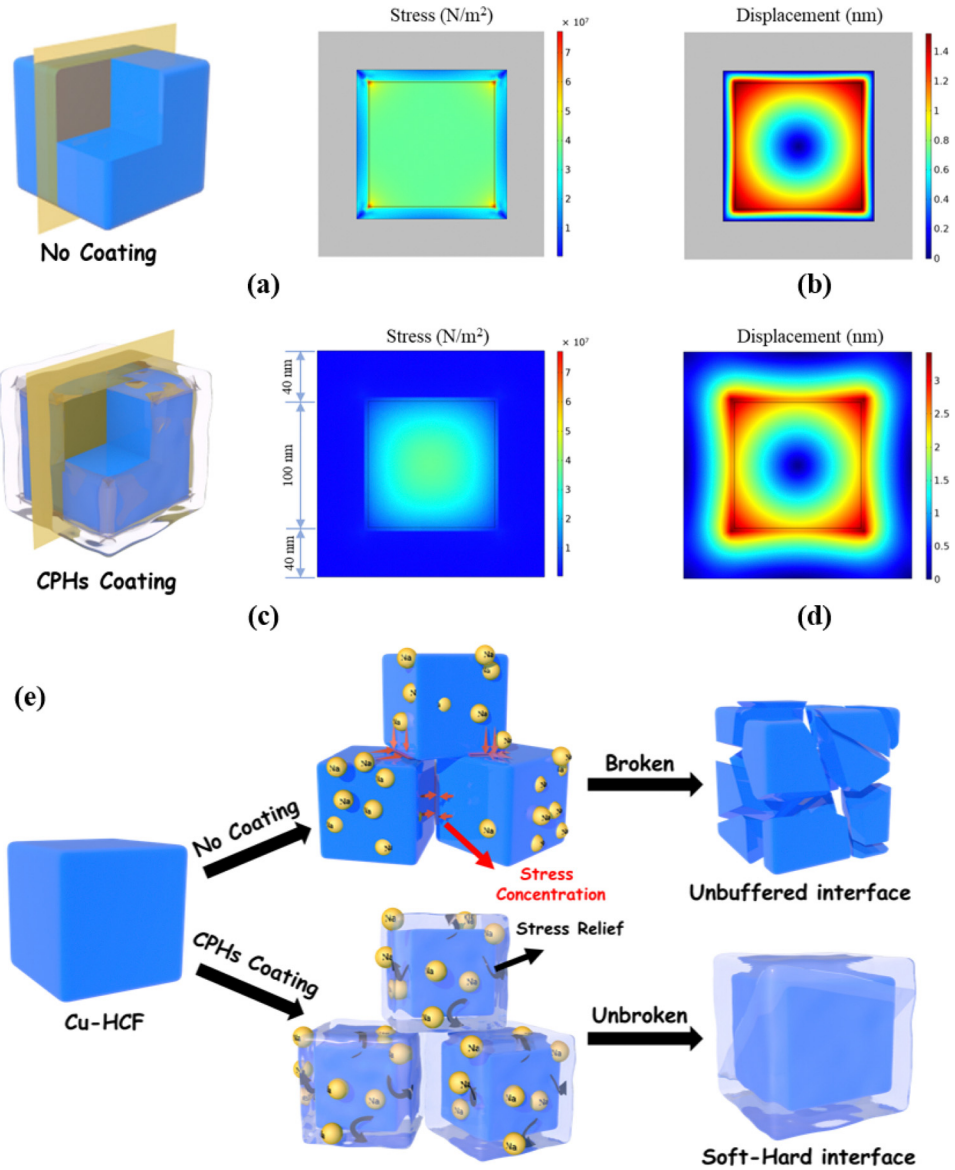

Fig. 6 Finite-element simulation results of stress and deformation displacement in (a and b) CuHCF and (c and d) CuHCF@PVA/PPy. (e) Schematic of buffer stress concentration in the soft–hard interface.

To further illustrate the buffering effect of the soft–hard interface in the process of ion intercalation, the finite-element simulation method was used to study the stress distribution and displacement changes that occur after the volume expansion of the uncoated layer and layers coated with gel (Fig. 6a–d). During the desalination process, the internal stress of the CuHCF without a coating layer is uniform after electrochemical volume expansion at 4×10^7 N m^{-2}. However, the darker colour at the four corners of the figure indicates a larger stress, which is caused by the shear stress generated by the ion intercalation process and the mutual contact of the particles at the edges (Fig. 6a).

CuHCF@PVA/PPy exhibits a relatively low stress (2.5×10^7 N m^{-2}), and the stress at the edge is significantly reduced (Fig. 6c). The surface of the CuHCF coated with CPHs generates a soft–hard interface, which can effectively absorb the stress generated during the reaction, thereby playing a buffering role. The displacement is used to represent the volume change in the material during ion intercalation. The contact area between the particles is small, owing to the uniform distribution and gel layer coating. Moreover, CuHCF@PVA/PPy exhibits a displacement of approximately 3 nm (Fig. 6d), and does not exhibit stress concentration during the volume expansion. In contrast, CuHCF with a larger stress concentration has a smaller displacement change (1.5 nm) owing to mutual accumulation and close contact. The stress concentration caused by the CuHCF lattice change during Na^+ insertion/de-intercalation cannot be alleviated, which eventually results in electrode cracking and deactivation (Fig. 6b). Therefore, CuHCF@PVA/PPy exhibits excellent structural integrity and a long lifetime, which enables high capacity and cycling stability for desalination (Fig. 6e).

 This journal is © The Royal Society of Chemistry 2023

Published on 22 Mart 2023. Downloaded on 12.05.2026 22:31:39.

Conclusion

In conclusion, we have prepared a CuHCF@PVA/PPy electrode material with excellent ECDI performance using the "soft–hard" interface design, which demonstrated an exceptional salt-adsorption capacity of 22.7 mg g^{-1} and good cyclic stability (90% after 100 cycles). The 3D layered PVA/PPy conductive polymers can control the particle size, alleviate nanoparticle aggregation, and improve the material utilisation efficiency. More importantly, the elastic modulus of the "soft structure" can improve the cyclability of the electrode because the hydrogel provides a cushion to accommodate the lattice strain between stacked particles caused during the Na^+ (de)intercalation. Additionally, the hydrogel can withstand considerable water flow and maintain its integral electrode structure during the desalination process, thereby maintaining stability. The preparation of CuHCF@PVA/PPy is simple and feasible, which is beneficial for realising the practical application of high-performance ECDI. Furthermore, the novel design of the CPHs provides a potential solution for the further development of faradaic electrode materials in ECDI.

Conflicts of interest

There are no conflicts to declare.

Acknowledgements

This study was supported by the National Natural Science Foundation of China (Grant No. 22276137 and 52170087), the JST-ERATO Yamauchi MaterialsSpace-Tectonics Project (JPMJER2003), and ITB Research Grant 308/IT1.B07.1/TA.01/2023. We are grateful to Dr Jinping Huang and his students from Shanghai Normal University for their help with *in situ* XRD testing. Dr Mingxing Liang provided suggestions and guidance for this manuscript. We are also thankful to the anonymous reviewers for their valuable comments that improved this manuscript. This work was performed in part at the Queensland node of the Australian National Fabrication Facility, a company established under the National Collaborative Research Infrastructure Strategy to provide nano and microfabrication facilities for Australia's researchers.

References

1 Y. Liu, K. Wang, X. Xu, K. Eid, A. M. Abdullah, L. Pan and Y. Yamauchi, *ACS Nano*, 2021, **15**, 13924–13942.
2 X. Xu, M. Eguchi, Y. Asakura, L. Pan and Y. Yamauchi, *Energy Environ. Sci.*, 2023, **16**, 1815–1820.
3 S. A. Hawks, A. Ramachandran, S. Porada, P. G. Campbell, M. E. Suss, P. M. Biesheuvel, J. G. Santiago and M. Stadermann, *Water Res.*, 2019, **152**, 126–137.
4 M. E. Suss, S. Porada, X. Sun, P. M. Biesheuvel, J. Yoon and V. Presser, *Energy Environ. Sci.*, 2015, **8**, 2296–2319.
5 Y.-H. Tu, Y.-H. Yang and C.-C. Hu, *Desalination*, 2021, **498**, 114807.
6 A. Suresh, G. T. Hill, E. Hoenig and C. Liu, *Mol. Syst. Des. Eng.*, 2021, **6**, 25–51.
7 Y.-H. Tu, Y.-C. Tai, J.-Y. Xu, Y.-H. Yang, H.-Y. Huang, J.-H. Huang and C.-C. Hu, *Desalination*, 2022, **538**, 115928.
8 J. C. Farmer, D. V. Fix, G. V. Mack, R. W. Pekala and J. F. Poco, *J. Electrochem. Soc.*, 1996, **143**, 159–169.
9 Y. C. Xiong, F. Yu, S. Arnold, L. Wang, V. Presser, Y. F. Ren and J. Ma, *Research*, 2021, 2021.
10 M. Pasta, C. D. Wessells, Y. Cui and F. La Mantia, *Nano Lett.*, 2012, **12**, 839–843.
11 Q. Li, Y. Zheng, D. J. Xiao, T. Or, R. Gao, Z. Q. Li, M. Feng, L. L. Shui, G. F. Zhou, X. Wang and Z. W. Chen, *Adv. Sci.*, 2020, **7**, 52.
12 J. Ma, Y. C. Xiong, X. H. Dai and F. Yu, *Environ. Sci. Technol. Lett.*, 2020, **7**, 118–125.
13 G. C. Tan, S. D. Lu, N. Xu, D. X. Gao and X. P. Zhu, *Environ. Sci. Technol.*, 2020, **54**, 5843–5852.
14 S. Vafakhah, L. Guo, D. Sriramulu, S. Z. Huang, M. Saeedikhani and H. Y. Yang, *ACS Appl. Mater. Interfaces*, 2019, **11**, 5989–5998.
15 W. H. Shi, X. Y. Liu, T. Q. Deng, S. Z. Huang, M. Ding, X. H. Miao, C. Z. Zhu, Y. H. Zhu, W. X. Liu, F. F. Wu, C. J. Gao, S. W. Yang, H. Y. Yang, J. N. Shen and X. H. Cao, *Adv. Mater.*, 2020, **32**, 1907404.
16 J. L. Cao, Y. Wang, L. Wang, F. Yu and J. Ma, *Nano Lett.*, 2019, **19**, 823–828.
17 A. J. Zhou, W. J. Cheng, W. Wang, Q. Zhao, J. Xie, W. X. Zhang, H. C. Gao, L. G. Xue and J. Z. Li, *Adv. Energy Mater.*, 2021, **11**, 2000943.
18 J. W. Nai and X. W. Lou, *Adv. Mater.*, 2019, **31**, 1706825.
19 B. Q. Wang, Y. Han, X. Wang, N. Bahlawane, H. G. Pan, M. Yan and Y. Z. Jiang, *iScience*, 2018, **3**, 110–133.
20 D. M. Sun, H. Wang, B. W. Deng, H. Zhang, L. Wang, Q. Wan, X. X. Yan and M. Z. Qu, *Carbon*, 2019, **143**, 706–713.
21 S. J. R. Prabakar, J. Jeong and M. Pyo, *RSC Adv.*, 2015, **5**, 37545–37552.
22 S. Y. Lee, J. Y. Park, H. J. Kim, Y. S. Lee and Y. I. Park, *J. Alloys Compd.*, 2022, **898**, 162952.
23 P. Wan, H. Xie, N. Zhang, S. Zhu, C. Wang, Z. Yu, W. Chu, L. Song and S. Wei, *Adv. Funct. Mater.*, 2020, **30**, 2002624.
24 L. Li, J. Meng, M. T. Zhang, T. X. Liu and C. Zhang, *Chem. Commun.*, 2021, **58**, 185–207.
25 X. T. Han, G. C. Xiao, Y. C. Wang, X. N. Chen, G. G. Duan, Y. Z. Wu, X. Gong and H. X. Wang, *J. Mater. Chem. A*, 2020, **8**, 23059–23095.
26 Y. Zhao, B. R. Liu, L. J. Pan and G. H. Yu, *Energy Environ. Sci.*, 2013, **6**, 2856–2870.
27 Y. Shi, X. Y. Zhou, J. Zhang, A. M. Bruck, A. C. Bond, A. C. Marschilok, K. J. Takeuchi, E. S. Takeuchi and G. H. Yu, *Nano Lett.*, 2017, **17**, 1906–1914.
28 Z. F. Wang, H. F. Li, Z. J. Tang, Z. X. Liu, Z. H. Ruan, L. T. Ma, Q. Yang, D. H. Wang and C. Y. Zhi, *Adv. Funct. Mater.*, 2018, **28**, 1804560.
29 B.-S. Yin, S.-W. Zhang, Q.-Q. Ren, C. Liu, K. Ke and Z.-B. Wang, *J. Mater. Chem. A*, 2017, **5**, 24942–24950.

Published on 22 Mart 2023. Downloaded on 12.05.2026 22:31:39.

30 M. F. Koudehi and S. M. Pourmortazavi, *Electroanalysis*, 2018, **30**, 2302–2310.
31 Z. M. Wang, X. T. Xu, J. Kim, V. Malgras, R. Mo, C. L. Li, Y. Z. Lin, H. B. Tan, J. Tang, L. K. Pan, Y. Bando, T. Yang and Y. Yamauchi, *Mater. Horiz.*, 2019, **6**, 1433–1437.
32 Z. Zhang, J.-G. Wang and B. Wei, *Nanomaterials*, 2017, **7**, 228.
33 X. Xu, J. Tang, Y. Kaneti, H. Tan, T. Chen, L. Pan, T. Yang, Y. Bando and Y. Yamauchi, *Mater. Horiz.*, 2020, **7**, 1404–1412.
34 X. K. Zhang, M. T. Xia, T. T. Liu, N. Peng, H. X. Yu, R. T. Zheng, L. Y. Zhang, M. Shui and J. Shu, *Chem. Eng. J.*, 2021, **421**, 9.
35 S.-H. Lee, M. Choi, J.-K. Moon, S.-W. Kim, S. Lee, I. Ryu, J. Choi and S. Kim, *Colloids Surf., A*, 2022, **647**, 129175.
36 C.-L. Yeh, H.-C. Hsi, K.-C. Li and C.-H. Hou, *Desalination*, 2015, **367**, 60–68.
37 M. Ding, K. K. Bannuru, Y. Wang, L. Guo, A. Baji and H. Y. Yang, *Adv. Mater. Technol.*, 2018, **3**, 1800135.
38 C. D. Wessells, R. A. Huggins and Y. Cui, *Nat. Commun.*, 2011, **2**, 550.
39 Z. Gan, J. Yin, X. Xu, Y. Cheng and T. Yu, *ACS Nano*, 2022, **16**, 5131–5152.
40 J. Shao, J. Feng, H. Zhou and A. Yuan, *Appl. Surf. Sci.*, 2019, **471**, 745–752.
41 M. X. Liang, L. Wang, V. Presser, X. H. Dai, F. Yu and J. Ma, *Adv. Sci.*, 2020, 7.
42 Y. Huang, F. Chen, L. Guo, J. Zhang, T. Chen and H. Y. Yang, *Desalination*, 2019, **451**, 241–247.
43 W. Zhao, M. Ding, L. Guo and H. Y. Yang, *Small*, 2019, **15**, 1805505.
44 Z.-Y. Yang, L.-J. Jin, G.-Q. Lu, Q.-Q. Xiao, Y.-X. Zhang, L. Jing, X.-X. Zhang, Y.-M. Yan and K.-N. Sun, *Adv. Funct. Mater.*, 2014, **24**, 3917–3925.
45 H. Wang, L. Shi, T. Yan, J. Zhang, Q. Zhong and D. Zhang, *J. Mater. Chem. A*, 2014, **2**, 4739–4750.
46 X. Xu, Y. Liu, T. Lu, Z. Sun, D. H. C. Chua and L. Pan, *J. Mater. Chem. A*, 2015, **3**, 13418–13425.
47 T. Yan, J. Liu, H. Lei, L. Shi, Z. An, H. S. Park and D. Zhang, *Environ. Sci.: Nano*, 2018, **5**, 2722–2730.
48 B. Chen, A. Feng, R. Deng, K. Liu, Y. Yu and L. Song, *ACS Appl. Mater. Interfaces*, 2020, **12**, 13750–13758.
49 W. Bao, X. Tang, X. Guo, S. Choi, C. Wang, Y. Gogotsi and G. Wang, *Joule*, 2018, **2**, 778–787.
50 W. Shi, X. Zhou, J. Li, E. R. Meshot, A. D. Taylor, S. Hu, J.-H. Kim, M. Elimelech and D. L. Plata, *Environ. Sci. Technol. Lett.*, 2018, **5**, 692–700.
51 H. Yin, S. Zhao, J. Wan, H. Tang, L. Chang, L. He, H. Zhao, Y. Gao and Z. Tang, *Adv. Mater.*, 2013, **25**, 6270–6276.
52 Z. Ding, X. Xu, Y. Li, K. Wang, T. Lu and L. Pan, *Desalination*, 2019, **468**, 114078.
53 X. Zhang and J. Dutta, *ACS Appl. Energy Mater.*, 2021, **4**, 8275–8284.
54 A. Amiri, Y. Chen, C. Bee Teng and M. Naraghi, *Energy Storage Mater.*, 2020, **25**, 731–739.
55 H. Wu, G. Yu, L. Pan, N. Liu, M. T. McDowell, Z. Bao and Y. Cui, *Nat. Commun.*, 2013, **4**, 1943.
56 Y.-H. Yang, Y.-H. Tu, H.-Y. Huang and C.-C. Hu, *Desalination*, 2023, **545**, 116160.
57 M. Haro, G. Rasines, C. Macias and C. O. Ania, *Carbon*, 2011, **49**, 3723–3730.
58 H. Zhang, C. Wang, W. Zhang, M. Zhang, J. Qi, J. Qian, X. Sun, B. Yuliarto, J. Na, T. Park, H. G. A. Gomaa, Y. V. Kaneti, J. W. Yi, Y. Yamauchi and J. Li, *J. Mater. Chem. A*, 2021, **9**, 12807–12817.
59 J. Lee, P. Srimuk, K. Aristizabal, C. Kim, S. Choudhury, Y.-C. Nah, F. Mücklich and V. Presser, *ChemSusChem*, 2017, **10**, 3611–3623.
60 T. Wu, G. Wang, S. Wang, F. Zhan, Y. Fu, H. Qiao and J. Qiu, *Environ. Sci. Technol. Lett.*, 2018, **5**, 98–102.
61 W. Zhao, L. Guo, M. Ding, Y. Huang and H. Y. Yang, *ACS Appl. Mater. Interfaces*, 2018, **10**, 40540–40548.
62 X. Shen, R. Hai, X. Wang, Y. Li, Y. Wang, F. Yu and J. Ma, *J. Mater. Chem. A*, 2020, **8**, 19309–19318.
63 L. Chen, X. Xu, L. Wan, G. Zhu, Y. Li, T. Lu, M. D. Albaqami, L. Pan and Y. Yamauchi, *Mater. Chem. Front.*, 2021, **5**, 3480–3488.
64 Y. Tang, Y. Zhang, O. I. Malyi, N. Bucher, H. Xia, S. Xi, Z. Zhu, Z. Lv, W. Li and J. Wei, *Adv. Mater.*, 2018, **30**, 1802200.
65 C. Chen, Y. Wen, X. Hu, X. Ji, M. Yan, L. Mai, P. Hu, B. Shan and Y. Huang, *Nat. Commun.*, 2015, **6**, 6929.
66 S. Vafakhah, L. Guo, D. Sriramulu, S. Huang, M. Saeedikhani and H. Y. Yang, *ACS Appl. Mater. Interfaces*, 2019, **11**, 5989–5998.

 This journal is © The Royal Society of Chemistry 2023